Two States of the Cathode Catalyst Layer Operation in a PEM Fuel Cell

Tatyana Reshetenko [1,*,z] **and Andrei Kulikovsky** [2,3,*,z]

[1] *Hawaii Natural Energy Institute, University of Hawaii, Honolulu, Hawaii 96822, USA*
[2] *Forschungszentrum Jülich GmbH, Institute of Energy and Climate Research, IEK–3: Electrochemical Process Engineering, D-52425 Jülich, Germany*
[3] *Lomonosov Moscow State University, Research Computing Center, 119991 Moscow, Russia*

We measure impedance of a standard Pt/C–based PEM fuel cell for a series of current densities from 50 to 400 mA cm^{-2}. Using our recent model for extraction of spatially–resolved data from impedance spectra, we plot the dependence of the oxygen diffusion coefficient D_{ox} in the cathode catalyst layer (CCL) and D_b in the gas–diffusion layer (GDL) on the distance along the cathode channel. While the GDL oxygen diffusivity is fairly uniform over the cell active area, the shape of D_{ox} indicates that the cell is separated into two domains with high and low water contents in the CCL. We attribute this effect to the positive feedback loop between the rates of oxygen transport and liquid water evaporation in the CCL, leading to local CCL flooding.
 [DOI: 10.1149/2.0541810jes]

Manuscript submitted May 2, 2018; revised manuscript received June 11, 2018. Published July 20, 2018.

Impedance spectroscopy becomes increasingly popular method of PEM fuel cell characterization. The database of scientific publications Scopus shows that a number of publications on theory and applications of electrochemical impedance spectroscopy (EIS) in fuel cells exhibits exponential growth (Figure 1). The characteristic time of the exponent is 7 years, which means that the number of publications on this topic doubles every 4 years and 10 months. This manifestation of the Moore's law is a signature of extremely powerful method.

A great advantage of EIS is the possibility to extract information on kinetic and transport coefficients in the cell components from the cell spectra. This, however, requires quite sophisticated physics–based modeling of the cell impedance.[1–12] Being fitted to an experimental spectrum, models of that type return oxygen diffusion coefficients in the porous layers, the cathode catalyst layer (CCL) proton conductivity, kinetic rate constants of the oxygen reduction reaction (ORR) etc.

Recently, we have shown that the spectrum of a fuel cell contains information on spatial distribution of the transport parameters over the cell active area.[13] To explain this effect, suppose that the cell is separated into N virtual segments. The impedance of each segment "knows" what is going on in the segments located upstream due to the oxygen flow in the cathode channel. This flow transports small–amplitude perturbations of the oxygen concentration from one segment to another, and in this way the total cell impedance contains information on the local transport and kinetic coefficients in each individual segment.

In this work, we extract the spatial shapes of the oxygen diffusion coefficient in the CCL D_{ox} from the experimental spectra of a standard PEM fuel cell. These shapes show that the cell active area is split into two distinct domains with high and low D_{ox}. We attribute this effect to the instability arising due to positive feedback loop between the rates of oxygen transport and liquid water evaporation in the CCL.

Experimental

Experimental work has been performed using a segmented cell system and a test station developed at Hawaii Natural Energy Institute (Figure 2). The segmented cell setup consists of the cell hardware, current transducer system and data acquisition device. The current transducer system was custom designed and employed closed loop Hall sensors (Honeywell CSNN191) for current measurements. The segmented cell system is run as a single cell using the test station and standard operating protocols. This configuration reduces any interferences from the segmented cell setup and provides operating conditions identical to real ones, since only the overall cell load is governed by the test station. The whole system enables simultaneous measurements of spatial current, voltage and impedance. Details of the segmented cell system can be found in Refs. 14,15.

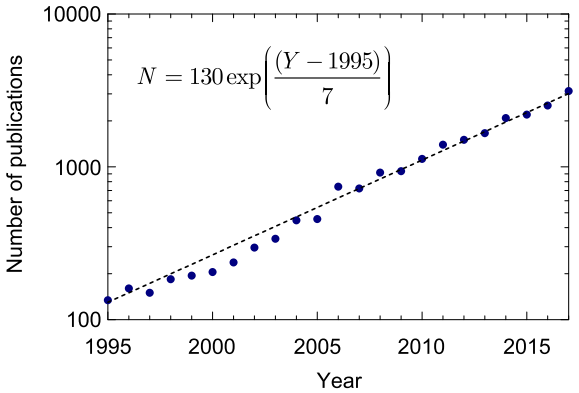

Figure 1. The number of publications on EIS in fuel science and technology vs time.

The segmented cell hardware contains standard non-segmented and segmented flow field plates and a 100 cm^2 MEA. The segmented flow field consists of 10 segments, each of them has an area of 7.6 cm^2, its own current collector and gas diffusion layer (GDL). The inlet segment is segment 1, while segment 10 is the cell outlet. The system design allows either anode or cathode to be segmented. In this work, the segmentation was applied to the cathode. Both flow field plates have the same ten parallel channel serpentine design. The fuel and oxidant streams are arranged in co-flow configuration.

We used commercially available 100 cm^2 catalyst coated membranes (CCM) provided by Gore. Pt loading was 0.4 mg$_{Pt}$ cm^{-2} for anode and cathode with the catalyst layer thickness of 10–12 μm. The thickness of the reinforced membrane varied in the range of 16–18 μm. Sigracet 25 BC was used as GDLs for both electrodes. 25 BC consists of carbon paper and a microporous layer (MPL) with total thickness of 220–235 μm and porosity of 80%. Segmented GDLs were used on the cathode side, whereas a single and uniform GDL was applied at the anode. Teflon gaskets (125 μm) were employed for both electrodes to ensure required compression ratio.

The cell was operated with H_2/air gas configuration at a temperature of 80°C. The anode/cathode conditions were 2/9.5 stoichiometry, 100/50% relative humidity and 150/150 kPa absolute pressure. The air stoichiometry of 9.5 has been taken to minimize nonuniformity of the oxygen concentration over the cell active area. The impedance

*Electrochemical Society Member.
[z]E-mail: tatyanar@hawaii.edu; A.Kulikovsky@fz-juelich.de

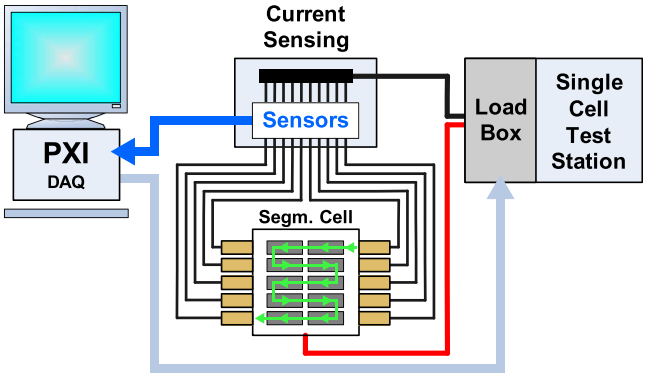

Figure 2. Sketch of the segmented cell and the experimental setup. *Reprinted from the publication by T. Reshetenko, G. Bender, K. Bethune, R. Rocheleau, Electrochim. Acta 56 (2011) 8700–8711 with permission from Elsevier.*[16]

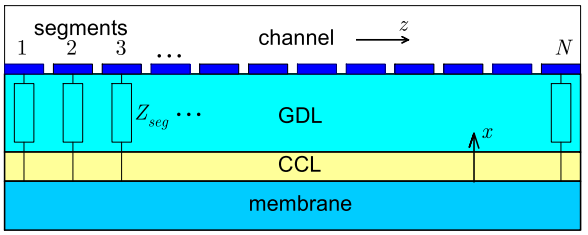

Figure 3. Schematic of the segmented cell and the system of coordinates.

measurements were performed under galvanostatic control of the cell over the frequency range from 0.05 Hz to 10 kHz with 11 steps per decade. The amplitude of the sinusoidal current perturbation signal was chosen to get a cell voltage response of 10 mV or lower. The impedance spectra have been recorded simultaneously from 10 segments and from the whole cell. In this work, we used only the whole cell spectra for processing. The cell operating and geometrical parameters are listed in Table I. Note that in our previous work,[13] we used a low–Pt loaded MEA with the Pt loading of 0.1 mg_{Pt} cm^{-2}; here, we perform experiments with the standard MEA from Gore having Pt loading of 0.4 mg_{Pt} cm^{-2}.

Model

Model equations and impedance.—The experimental segmented cell with the meander–like channel (Figure 2) is modeled below as a segmented cell with the single straight channel (Figure 3). The experimental spectra have been fitted using the physics–based model for PEMFC impedance;[13,15] the model is based on the following idea.

The impedance model is obtained from the system of through–plane conservation equations in the individual segment; the boundary condition for the oxygen concentration perturbation in each segment is derived from the oxygen mass transport equation in the channel. In this way, individual segments are linked by the oxygen transport in the channel. The through–plane model includes the proton charge conservation Equation 1, the Ohm's law 2, and the oxygen mass transport equations in the CCL 3, and in the GDL 4:

$$C_{dl}\frac{\partial \eta}{\partial t}+\frac{\partial j}{\partial x}=-i_*\left(\frac{c}{c_h^{in}}\right)\exp\left(\frac{\eta}{b}\right) \quad [1]$$

$$j=-\sigma_0\exp(-\beta x/l_t)\frac{\partial \eta}{\partial x} \quad [2]$$

$$\frac{\partial c}{\partial t}-D_{ox}\frac{\partial^2 c}{\partial x^2}=-\frac{i_*}{4F}\left(\frac{c}{c_h^{in}}\right)\exp\left(\frac{\eta}{b}\right) \quad [3]$$

$$\frac{\partial c_b}{\partial t}-D_b\frac{\partial^2 c_b}{\partial x^2}=0 \quad [4]$$

The oxygen transport in the channel is described by the mass transport equation assuming plug flow:

$$\frac{\partial c_h}{\partial t}+v\frac{\partial c_h}{\partial z}=\frac{N_b}{h} \quad [5]$$

where

$$N_b=-D_b\left.\frac{\partial c_b}{\partial x}\right|_{x=l_t+l_b} \quad [6]$$

is the local oxygen flux on the GDL side of the channel/GDL interface. Here, c, c_b, c_h are the oxygen concentrations in the CCL, GDL and channel, respectively, x and z are the coordinates through the cathode and along the channel, respectively, c_h^{in} is the reference (inlet) oxygen concentration, C_{dl} is the double volumetric layer capacitance, D_{ox}, D_b are the oxygen diffusion coefficients in the CCL and the GDL, respectively, h is the channel depth, i_* is the ORR volumetric exchange current density, b is the ORR Tafel slope, σ_0 is the CCL proton conductivity at the membrane interface, β is the inverse characteristic scale of the proton conductivity decay toward the GDL, l_t, l_b are the CCL and the GDL thickness, respectively, L is the channel length, and v is the air flow velocity. Note that the MEA used exhibits a strong decay of the CCL proton conductivity with the distance through the CCL depth; this effect is taken into account by the exponential factor in Eq. 2 with $\beta = 7.3$.[17]

Following the procedure of impedance measurements, we apply a small–amplitude perturbation of potential to all the segments. Equations 3–5 are nondimensionalized, linearized, and Fourier–transformed to obtain a linear system of equations for the small perturbation amplitudes of the overpotential $\tilde{\eta}^1$ and the oxygen concentrations $\tilde{c}^1$, $\tilde{c}_b^1$ and $\tilde{c}_h^1$ in the ω–space. Here, the superscript 1 marks the small–amplitude perturbations, and the sign tilde marks the dimensionless variables. The cell impedance is calculated in a following way.

First, we split the cell into N virtual segments. The variable $\tilde{c}_h^1$ appears in the boundary condition for the through–plane system of equations along the $\tilde{x}$–coordinate. Suppose that the shape of $\tilde{c}_h^1$ along the channel is known; this allows us to calculate the impedance of each individual segment using the 1D through–plane impedance model.[18] The procedure returns also the shape of the oxygen flux perturbation $\tilde{N}_b^1$ at the channel/GDL interface along $\tilde{z}$, which stands as the sink term in the linearized version of Eq. 5. Solving the latter equation we get the updated profile of $\tilde{c}_h^1$, and repeat the procedure of calculation of segment impedances. These iterations are performed until the desired accuracy of the total cell impedance

$$\frac{1}{\tilde{Z}_{cell}}=\frac{1}{N}\sum_{n=1}^{N}\frac{1}{\tilde{Z}_{seg,n}} \quad [7]$$

is achieved. Here, $\tilde{Z}_{seg,n}$ is the dimensionless impedance of the nth segment.

The key feature of the model is that each segment is allowed to have its own set of the transport and kinetic parameters. The local through–plane impedance model is based on Eqs. 1–4 and in each segment it

Table I. Geometrical and operating parameters of the cell. A/C stands for anode/cathode.

Catalyst loading A/C, mg_{Pt} cm^{-2}	0.4/0.4
Catalyst layer thickness l_t, μm	12
Gas diffusion layer thickness l_b, μm	235
Channel depth h, cm	0.15
Channel length L, cm	52.78
ORR exchange current density i_*, A cm^{-3} (assumed)	10^{-3}
Flow stoichiometry A/C	2/9.5
Relative humidity A/C	100%/50%
Absolute pressure, A/C, kPa	150/150
Cell temperature, K	273 + 80

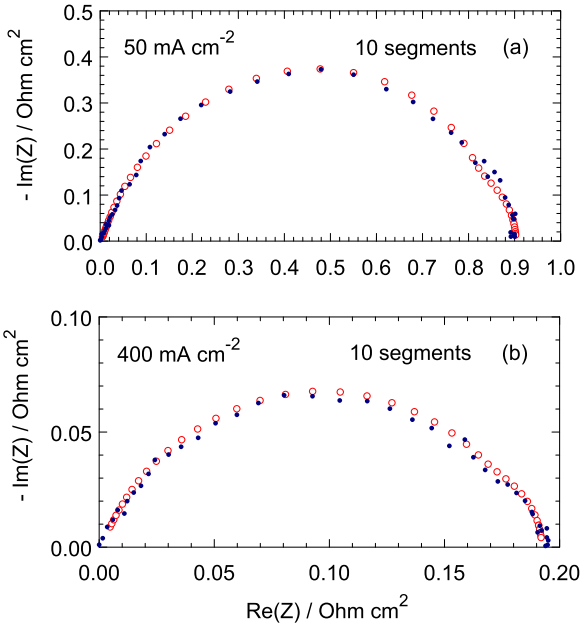

Figure 4. Experimental (dots) and fitted model (open points) spectra for the current density of (a) 50 mA cm^{-2} and (b) 400 mA cm^{-2}. The experimental and model points are shown for the same frequencies.

includes five parameters: the ORR Tafel slope b, the CCL oxygen diffusivity D_{ox} and proton conductivity σ_p, the double layer capacitance C_{dl}, and the oxygen diffusion coefficient D_b in the GDL. Thus, for the cell divided into 10 virtual segments, we get a least–squares problem with 50 parameters. Thanks to extremely powerful fitting algorithms available nowadays, this problem can be solved yielding the shapes of the aforementioned parameters along the channel.

Numerical details.—Spectra fitting has been performed using a self–written Python code invoking the *least_squares* procedure from the SciPy library. The boundary–value problems for the perturbation amplitudes and for the static shapes have been solved using the SciPy *solve_bvp* procedure. The Cauchy problem for the oxygen perturbation amplitude in the channel has been solved with the SciPy *odeint* solver.

The fitting has been performed in two steps. First, the spectrum has been fitted assuming that all the fitting parameters (b, C_{dl}, σ_p, D_{ox} and D_b) are uniform along the cathode channel. In the second step, the problem has been solved with variable along the z–coordinate parameters, taking the values obtained in the first step as initial conditions for *least_squares* internal iterations. To reduce the time of calculations, a parallel version of the code has been written, which employs a multi–core structure of modern processors for PC. On a 2.4 GHz PC with the quad–core processor fitting took about 3 hours per spectrum.

Results and Discussion

The cell geometrical and operating parameters used in the calculations are listed in Table I. The experimental and fitted model spectra for the current densities of 50 mA cm^{-2} and 400 mA cm^{-2} are shown in Figure 4. The calculated shapes of the oxygen diffusion coefficient in the CCL along the channel coordinate for the current densities of 50, 100, 200, 300 and 400 mA cm^{-2} are shown in Figure 5. For each current density, this Figure depicts the two shapes corresponding to the variants with 10 and 20 virtual segments. The respective shapes are close to each other, which confirms good quality of the model. For comparison, the values of D_{ox} obtained under the assumption of uniform cell parameters along the cathode channel are also shown.

Most interesting is that at the current densities of 100 to 400 mA cm^{-2}, the cell active area is split into two well–separated

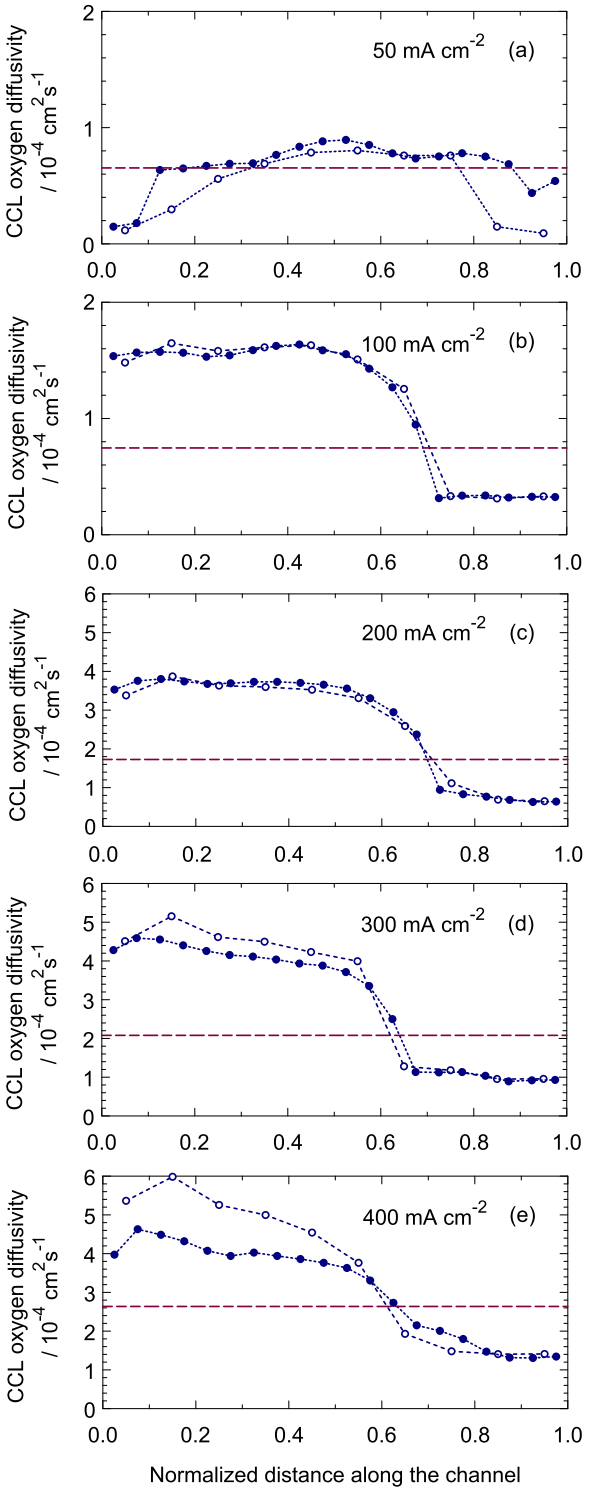

Figure 5. Calculated shapes of the CCL oxygen diffusivity D_{ox} along the air channel coordinate for the variants with 10 (open circles) and 20 (filled circles) virtual segments. Long–dashed straight lines show the values of D_{ox} obtained under the assumption of uniform cell parameters along the cathode channel.

domains with high and low D_{ox} (Figures 5b–5e). In the following discussion we will refer to the variant with 10 virtual segments. The last three segments 8–10 operate at D_{ox}, which is several times less than D_{ox} in the segments 1 to 7. At the cell current of 200 mA cm^{-2}, the ratio of the high to low D_{ox} is nearly 10 (Figure 5c). The only plausible explanation of this effect is flooding: the CCL in the last three segments works under severe flooding conditions.

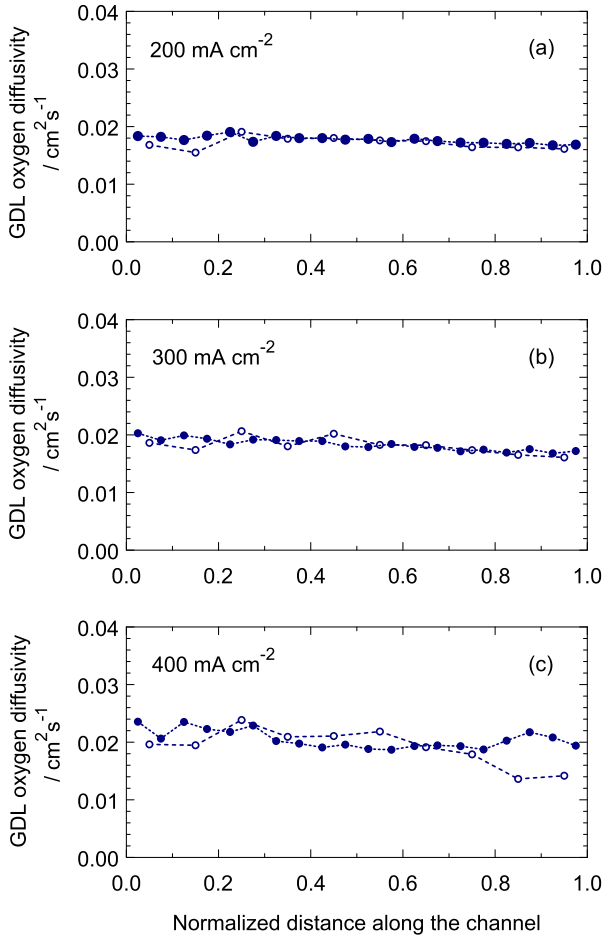

Figure 6. Calculated shapes of the GDL oxygen diffusivity D_b along the air channel coordinate for the variants with 10 (open circles) and 20 (filled circles) virtual segments.

Amazingly, the GDL in the segments 8 to 10 is not flooded and the GDL oxygen diffusivity does not change with the cell current density (Figure 6). Note that the local cell current density is nearly uniform along the cathode channel; the decay of D_{ox} in the last three segments does not lower the local current there (Figure 7). Furthermore, the distribution of the high–frequency resistance also does not show any significant decay in the last segments (Figure 8). Since the largest contribution to the HFR gives the membrane resistance, we conclude that the membrane water content exhibits only a minor variation along the channel. Flooding in the segments 8 to 10, thus, affects only the catalyst layer.

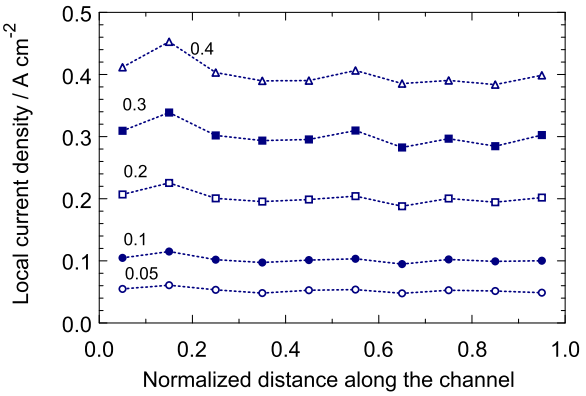

Figure 7. Measured local current density distribution along the cathode channel for the indicated values of the mean current density in the cell.

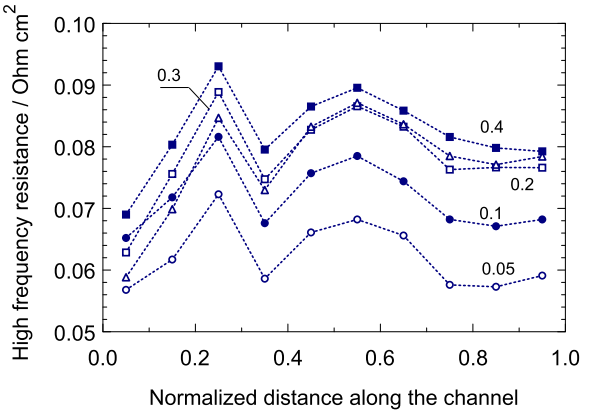

Figure 8. Measured distribution of the high–frequency resistance along the cathode channel for the indicated values of the mean current density in the cell.

To explain this effect we note that the key parameter describing operation of a partially flooded CCL is the reaction penetration depth l_{ox} due to oxygen transport[19]

$$l_{ox} = \frac{4FD_{ox}c_1}{j_0} \qquad [8]$$

where c_1 is the oxygen concentration at the CCL/GDL interface, and j_0 is the local cell current density. The regime of the CCL operation is determined by relation between l_{ox} and the CCL thickness l_t. If $l_{ox} \gg l_t$, oxygen easily penetrates through the CCL and the shape of the ORR rate through the CCL depth is determined by proton transport. If the proton transport is fast, the ORR rate is uniform through the CCL depth, otherwise this rate peaks at the membrane surface.

In the opposite limit of $l_{ox} < l_t$, the ORR runs mainly at the CCL/GDL interface, as the oxygen does not penetrate deep into the CCL. This regime is sketched in Figure 9 for the case of $l_{ox}/l_t \simeq 0.4$. As can be seen, about 60% of the CCL thickness adjacent to the membrane is inactive: in this domain, the ORR rate is close to zero and hence the proton current density does not change (Figure 9). The effective CCL volume is, thus, reduced by the factor of $\simeq 0.4$.

On the other hand, liquid water produced in the ORR must be evaporated in–place to provide "clean" pathway for gaseous transport of oxygen. The total rate of water evaporation in the CCL is proportional to the active CCL volume (Eq. 5 in Refs. 20 and 21). Estimates of Eikerling[20] show that at a normal operating regime with $l_{ox} > l_t$, a standard 10–μm CCL is able to evaporate all liquid water produced in the ORR up to the cell current density on the order of 1 A cm^{-2}. However, reduction of the effective CCL depth lowers the CCL evaporation efficiency, which may lead to catalyst layer flooding. In terms of

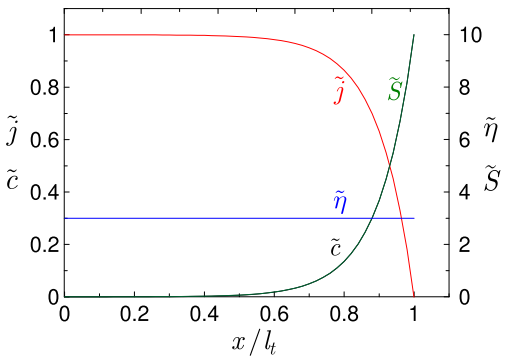

Figure 9. Schematic of the CCL operation at low reaction penetration depth due to poor oxygen diffusion, Eq. 8. Shown are the dimensionless shapes of the proton current density $\tilde{j}$, the local ORR overpotential $\tilde{\eta}$, the oxygen concentration $\tilde{c}$ and the ORR rate $\tilde{S}$. Fast proton transport is assumed, which translates into uniform profile of $\tilde{\eta}$. The ratio $l_{ox}/l_t \simeq 0.4$ is assumed.

Figure 9, the remaining in operation 40%–part of the CCL is not able to evaporate all liquid water produced in the ORR and it is flooded. (It is worth noting that the CCL with reduced catalyst loading and thereby lower depth is more prone to flooding.)

The data in Table I and in Figures 5, 6 allow us to estimate l_{ox} in the flooded domain. The oxygen concentration at the CCL/GDL interface is $c_1 = c_h^{in}(1 - j_0/j_{lim})$, where $j_{lim} = 4FD_b c_h^{in}/l_b$ is the limiting current density due to oxygen transport in the GDL. With the data in Table I, and $D_b \simeq 0.02\,\text{cm}^2\,\text{s}^{-1}$ (Figure 6), for $j_0 = 0.2\,\text{A cm}^{-2}$ we get $c_1 \simeq 8.5 \cdot 10^{-6}\,\text{mol cm}^{-3}$. With this c_1 and $D_{ox} \simeq 0.7 \cdot 10^{-4}\,\text{cm}^2\,\text{s}^{-1}$ (Figure 5c, segments 8 –10), from Eq. 8 for the same current density we obtain $l_{ox} = 0.0012$ cm. The CCL thus operates in the transition regime with $l_{ox} \simeq l_t$, which means quite a noticeable decay of the oxygen concentration c through the CCL depth: assuming exponential decay of c toward the membrane, $c \sim \exp(-x/l_{ox})$, (Eq. (22) in Ref. 19) c_0 at the membrane interface is nearly 3 times less than c_1 at the CCL/GDL interface. This decay shifts the ORR peak to the CCL/GDL interface and it lowers the effective volume for the liquid water evaporation.

This estimate does not take into account possible lowering of local CCL temperature close to the channel outlet. This may further contribute to lowering of CCL evaporation performance in the last segments, which appears to be insufficient already at $j_0 = 100\,\text{mA cm}^{-2}$ (Figure 5b). Note that in the non–flooded domain of the cell (segments 1 to 7), l_{ox} is five to ten times larger and hence in this domain the relation $l_{ox} \gg l_t$ holds.

The positive feedback loop between the CCL oxygen diffusivity D_{ox} and the evaporation rate could, therefore, lead to instability of the CCL operation. Indeed, lowering of D_{ox} reduces the oxygen penetration depth into the electrode, thereby reducing the effective volume of liquid water evaporation, which leads to higher liquid water saturation in the CCL. This, in turn, translates into lower D_{ox}, which further reduces the water evaporation rate. As a result, the cell active area appears to be split into two domains with the low and high water contents in the catalyst layer. Moreover, the experiment shows that this two–domain configuration is stable with respect to variation of the cell current density (Figure 5). It should be emphasized that by *instability* we mean the mechanism leading to the two separated in space stable domains of the CCL operation. We have no direct experimental evidences for transient functioning of this mechanism; however, the fact that the cell active area is separated into two domains with the non–flooded and flooded CCL is a clear consequence of this transient.

The instability discussed is a critical phenomenon: it does not happen when $l_{ox} \gg l_t$, and it starts to develop as soon as the relation $l_{ox} \simeq l_t$ holds. It is, thus, important to keep l_{ox} two to three times larger than l_t during the cell operation. Interestingly, the process of CCL flooding does not affect the GDL transport properties (Figure 6).

Conclusions

We use our recent model to extract spatially resolved oxygen diffusion coefficients in the catalyst D_{ox} and gas–diffusion D_b layers from the impedance spectra of a PEM fuel cell measured at the cell current densities in the range of 50 to 400 mA cm^{-2}. The shape of D_{ox} along the oxygen channel shows that the cell active area is split into two domains with high and low D_{ox}. We attribute this effect to insufficient capability of CCL to evaporate liquid water produced in the ORR in the domain close to the channel outlet. Flooding of this domain of the cell occurs due to positive feedback loop between the oxygen diffusivity and the rate of liquid water evaporation in the CCL. Decrease in D_{ox} reduces the active volume of the CCL, which, in turn, lowers the total rate of water evaporation in the layer. In the flooded domain, the reaction penetration depth due to oxygen transport in the CCL appears to be close to the CCL thickness, which provides conditions for the development of oxygen transport – water evaporation instability.

Acknowledgments

T. Reshetenko gratefully acknowledges funding from US Office of Naval Research (N00014-15-1-0028) and US Army Research Office (W911NF-15-1-0188). The authors are thankful to Günter Randolf and Jack Huizingh for valuable help in the system operation and the Hawaiian Electric Company for ongoing support of the Hawaii Sustainable Energy Research Facility.

List of Symbols

b	ORR Tafel slope, V
c	Oxygen molar concentration, mol cm^{-3}
c_h^{in}	Reference oxygen concentration (at the channel inlet), mol cm^{-3}
C_{dl}	Double layer volumetric capacitance, F cm^{-3}
D_b	Effective oxygen diffusion coefficient in the GDL, cm^2 s^{-1}
D_{ox}	Effective oxygen diffusion coefficient in the CCL, cm^2 s^{-1}
f	Regular frequency, Hz
F	Faraday constant, C mol^{-1}
h	Channel depth, cm
i	Imaginary unit
i_*	Volumetric exchange current density, A cm^{-3}
j_0	Local cell current density, A cm^{-2}
J	Mean cell current density, A cm^{-2}
l_b	GDL thickness, cm
l_{ox}	Characteristic oxygen penetration depth, cm
l_t	Catalyst layer thickness, cm
L	Channel length,cm
t	Time, s
v	Flow velocity in the cathode channel, cm s^{-1}
x	Coordinate through the cell, cm
z	Coordinate along the air channel, cm
Z_{cell}	Cell impedance, Ω cm^2
Z_{seg}	Local impedance of the segment, Ω cm^2

Greek

β	Characteristic parameter of σ_p decay along x, Eq. 2
λ	Air flow stoichiometry
σ_p	CCL proton conductivity, Ω^{-1} cm^{-1}
σ_0	CCL ionic conductivity at the membrane surface, Ω^{-1} cm^{-1}
ω	Angular frequency ($\omega = 2\pi f$), s^{-1}

Subscripts

0	Membrane/CCL interface
1	CCL/GDL interface
b	GDL
h	Air channel
t	Catalyst layer

Superscripts

1	Small–amplitude perturbation

ORCID

Tatyana Reshetenko https://orcid.org/0000-0002-4552-062X
Andrei Kulikovsky https://orcid.org/0000-0003-1319-576X

References

1. T. E. Springer, T. A. Zawodzinski, M. S. Wilson, and S. Gottesfeld, Characterization of polymer electrolyte fuel cells using AC impedance spectroscopy, *J. Electrochem. Soc.*, **143**, 587 (1996).
2. Y. Bultel, L. Genies, O. Antoine, P. Ozil, and R. Durand, Modeling impedance diagrams of active layers in gas diffusion electrodes: Diffusion, ohmic drop effects and multistep reactions, *J. Electroanal. Chem.*, **527**, 143 (2002).

3. F. Jaouen and G. Lindbergh, Transient techniques for investigating mass–transport limitations in gas diffusion electrode, *J. Electrochem. Soc.*, **150**, A1699 (2003).
4. Q. Guo and R. E. White, A steady–state impedance model for a PEMFC cahode, *J. Electrochem. Soc.*, **151**, E133 (2004).
5. Y. Bultel, K. Wiezell, F. Jaouen, P. Ozil, and G. Lindbergh, Investigation of mass transport in gas diffusion layer at the air cathode of a PEMFC, *Electrochimica Acta*, **51**, 474 (2005).
6. D. Gerteisen, A. Hakenjos, and J. O. Schumacher, AC impedance modeling study on porous electrodes of proton exchange membrane fuel cells using an agglomerate model, *J. Power Sources*, **173**, 346 (2007).
7. A. A. Franco, P. Schott, C. Jallut, and B. Maschke, A multi-scale dynamic mechanistic model for the transient analysis of PEFCs, *Fuel Cells*, **7**, 99 (2007).
8. M. Cimenti, D. Bessarabov, M. Tam, and J. Stumper, Investigation of proton transport in the catalyst layer of PEM fuel cells by electrochemical impedance spectroscopy, *ECS Transactions*, **28**(23), 147 (2010).
9. I. A. Schneider, M. H. Bayer, and S. von Dahlen, Locally resolved electrochemical impedance spectroscopy in channel and land areas of a differential polymer electrolyte fuel cell, *J. Electrochem. Soc.*, **158**, B343 (2011).
10. O. Shamardina, M. S. Kondratenko, A. V. Chertovich, and A. A. Kulikovsky, A simple transient model for a high temperature PEM fuel cell impedance, *Int. J. Hydrogen Energy*, **39**, 2224 (2014).
11. B. P. Setzler and Th. F. Fuller, A physics–based impedance model of proton exchange membrane fuel cells exhibiting low–frequency inductive loops, *J. Electrochem. Soc.*, **162**, F519 (2015).
12. C. Bao and W. G. Bessler, Two–dimensional modeling of a polymer electrolyte membrane fuel cell with long flow channel. Part II. physics–based electrochemical impedance analysis, *J. Power Sources*, **278**, 675 (2015).
13. T. Reshetenko and A. Kulikovsky, A model for extraction of spatially resolved data from impedance spectrum of a PEM fuel cell, *J. Electrochem. Soc.*, **165**, F291 (2018).
14. A. Kulikovsky and O. Shamardina, A model for PEM fuel cell impedance: Oxygen flow in the channel triggers spatial and frequency oscillations of the local impedance, *J. Electrochem. Soc.*, **162**, F1068 (2015).
15. T. Reshetenko and A. Kulikovsky, Impedance spectroscopy characterization of oxygen transport in low– and high–pt loaded pem fuel cells, *J. Electrochem. Soc.*, **164**, F1633 (2017).
16. T. Reshetenko, G. Bender, K. Bethune, and R. Rocheleau, *Electrochim. Acta*, **56**, 8700 (2011).
17. T. Reshetenko and A. Kulikovsky, Impedance spectroscopy study of the PEM fuel cell cathode with nonuniform nafion loading, *J. Electrochem. Soc.*, **164**, E3016 (2017).
18. T. Reshetenko and A. Kulikovsky, Variation of PEM fuel cell physical parameters with current: Impedance spectroscopy study, *J. Electrochem. Soc.*, **163**(9), F1100 (2016).
19. A. A. Kulikovsky, The regimes of catalyst layer operation in a fuel cell, *Electrochimica Acta*, **55**, 6391 (2010).
20. M. Eikerling, Water management in cathode catalyst layers of PEM fuel cells, *J. Electrochem. Soc.*, **153**, E58 (2006).
21. T. Muzaffar, T. Kadyk, and M. Eikerling, Tipping water balance and the Pt loading effect in polymer electrolyte fuel cells: A model–based analysis, *Sustainable Energy & Fuels*, **2**, 1189 (2018).